Structural and Mechanical Behavior of Al-4.4Cu/2TiB_2 *In-Situ* Nanocomposites Fabricated by Post-*In-Situ* Reaction Ultrasonic Processing

JAYAKRISHNAN NAMPOOTHIRI, I. BALASUNDAR, T. RAGHU, and K.R. RAVI

Al-4.4Cu/TiB_2 composites were fabricated with and without post-*in-situ* reaction ultrasonic melt treatment. The structural and mechanical behaviors of the composites in both the as-cast (F) and T6—peak-aged conditions were analyzed and compared with the base alloy Al-4.4Cu. The microstructural result reveals that the ultrasonic-assisted processing enhanced the dispersion of nano-sized TiB_2 particles. The ultrasonic treatment-assisted fabrication has improved the yield strength of Al-4.4Cu/2TiB_2 composite about ~ 2 times over the monolithic Al-4.4Cu alloy in both the as-cast and peak-aged condition while retaining > 90 pct ductility of the matrix alloy. The various strengthening mechanisms operating in the materials, namely, base alloy, micro- and nanocomposite were discussed and the theoretical yield strength was estimated using appropriate equations. The theoretical yield strength estimates were found to correlate well with the experimental observations.

https://doi.org/10.1007/s11663-019-01713-x

I. INTRODUCTION

THE high specific modulus, strength, and its higher potential towards structural and transportation applications actuated significant research enthusiasm for Aluminum matrix composites.[1,2] Nevertheless, some of their mechanical properties, especially fracture toughness and ductility, still miss the mark concerning the necessities for large-scale fabrications.[3] Casati and Vedani[4] were envisioned that the shortcomings of MMCs like poor ductility, machinability, and fracture toughness could be surmounted by downsizing the reinforcement particles to nano-scale, *i.e.,* by the producing metal matrix nanocomposites (MMNCs). Henrique *et al.*[5] and Nie *et al.*[6] suggested that uniform dispersion or distribution of nanoparticles is an essential prerequisite to enhance the properties of the matrix alloy. However, the high surface activity of nanoparticles can lead to their agglomeration in the matrix while preparing such composites.[7,8] Of late, Yuan *et al.*[9] reported that ultrasonic (UT)-assisted casting techniques are advantageous to break the agglomerates and disperse the nano-reinforcement particles uniformly in the matrix. Studies by Estruga *et al.*[10] and Raghu *et al.*[11] reported that ultrasonic treatment is an effective tool to synthesize *in-situ* nanoparticles. *In-situ* particles have added advantages like improved wettability, thermal stability, and better interface bonding that provides effective load transfer characteristics.[12,13] In an earlier work, the authors have demonstrated that post-*in-situ* reaction ultrasonic treatment of conventional salt-melt route Al/TiB_2 composite can be used to fabricate TiB_2 nanoparticles of < 100 nm in size and concomitantly it breaks the agglomerates and improves the dispersion of particles effectively in the matrix of the composites.[14,15] Post-*in-situ* melt treatment method can alleviate the contamination of the melt due to dissolution of sonotrode material used for ultrasonic treatment during the salt-melt reaction.[16] Though post-*in-situ* melt technique has been proved to be advantageous, no systematic study has been carried out to understand the role of post-*in-situ* reaction on the reinforcement size, its distribution, grain refinement, and the precipitation hardening behavior of MMNCs so produced. Moreover, structure–property correlation studies on Al/TiB_2 composites fabricated *via* post-*in-situ* reaction ultrasonic

JAYAKRISHNAN NAMPOOTHIRI is with the Structural Nanomaterials Lab, PSG Institute of Advanced Studies, Coimbatore 641004, India and also with the Department of Production Engineering, PSG College of Technology, Coimbatore 641004, India. I. BALASUNDAR and T. RAGHU are with the Near Net Shape Group, Aeronautical Materials Division, Defence Metallurgical Research Laboratory, Hyderabad 500058, India. K.R. RAVI is with the Structural Nanomaterials Lab, PSG Institute of Advanced Studies and also with the Department of Metallurgical and Materials Engineering, Indian Institute of Technology Jodhpur, Jodhpur 342037, India. Contact e-mail: ravikr@iitj.ac.in

Manuscript submitted May 4, 2019.
Article published online November 1, 2019.

treatment are also limited. To address these issues, a comprehensive study on the effect of various parameters like reinforcement particle size, its dispersion, secondary phases, grain size, and precipitation hardening on mechanical properties of Al-4.4Cu/2wt pct TiB_2 nanocomposite has been carried out in the current work. The strengthening mechanisms in the Al-4.4Cu/2wt pct TiB_2 nanocomposite also have been investigated and discussed in detail.

II. EXPERIMENTAL METHODS

Al-4.4Cu alloy was prepared by melting pure aluminum (99.8 pct) and pure copper (99.7 pct) in a resistance furnace. The K_2TiF_6 and KBF_4 salts were mixed properly to achieve the stoichiometry composition that corresponds to the formation of 2 wt pct TiB_2 particles. The salt mixture was then preheated to 150 °C for 1 hour and added directly to 1 kg of Al-4.4Cu melt that was held at 800 °C. The melt was stirred using a coated graphite rod at regular intervals of 10 minutes. The melt was held at 800 °C for 60 minutes after salt mixture addition to ensure that the required reaction to form the TiB_2 proceeds to completion. The slag and dross present on the melt surface were removed and the remaining molten metal was then cast using a cast iron mold preheated at 400 °C (Schematic given in Figure 1). The material so cast will be referred to as composite without ultrasonic treatment.

Al-4.4Cu/2TiB_2 composite prepared by the aforementioned salt-melt reaction was re-melted in a clay-graphite crucible and then subjected to ultrasonic treatment at 750 °C. A high power ultrasonic generator (M/s. Hangzhou Success, China) fitted with a Ti-6Al-4V sonotrode was used to generate and transmit the ultrasound waves. The ultrasonic treatment was performed at an operating power of 1.75 kW, 20.1 kHz frequency for a period of five minutes and then cast. Earlier work on the system by the authors had revealed that 5-minute duration of ultrasonic treatment has resulted in lower particle size and better distribution.[16] Hence, the same has been used for the current study. The material will henceforth be referred as composite with ultrasonic treatment.

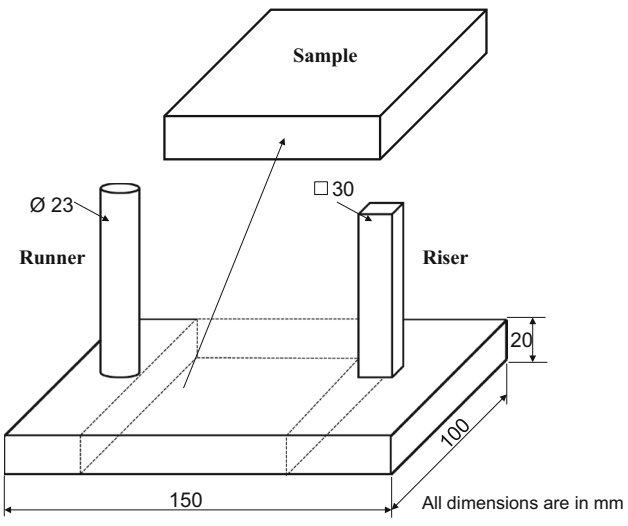

Fig. 1—Schematic of mold used for casting.

In order to study the influence of particles on precipitation hardening and mechanical properties, the base material (Al-4.4Cu) and the composite prepared without and with ultrasonic treatment were subjected to solutionizing and precipitation hardening treatments. Solutionizing was carried out at 540 °C for 6 hours followed by ice water quenching. The base alloy, Al-4.4Cu, was aged at 160 °C for 80 hours which is the recommended peak aging condition for the alloy. The Al-4.4Cu/TiB_2 composites prepared with and without ultrasonic treatment were peak aged at 160 °C for 36 and 52 hours, respectively.

From the cast material, samples were extracted and subjected to mechanical polishing following standard procedures. The polished samples were electrolytically etched using 2 pct HBF_4 solution and examined using Carl Zeiss Axioscope A1 microscope. Distributions of reinforcement particle in the untreated and ultrasonic-treated composite samples were analyzed using Field Emission Scanning Electron Microscopy (M/s Carl Zeiss, Sigma, UK). The size and shape of reinforcement particles and secondary phases were analyzed using Transmission Electron Microscopy (M/s. JEOL, JEM 2100, Japan) operating at 200 kV. For TEM, samples were sliced to ≤ 100 μm using a precision saw. The thin samples of composites were further thinned using twin-jet electro-polisher. A jet of perchloric acid was impinged on the TEM foil to remove the material. TEM analysis of base alloy and the composites with and without UT were also performed from the peak-aged samples to identify the size, morphology, and inter-precipitate spacing.

Standard tensile samples of 5 mm diameter with 30 mm gauge length were prepared out of the base alloy (Al-4.4Cu) and Al-4.4Cu/TiB_2 composites with and without ultrasonic treatment (UT). The samples were then tested at room temperature using a computer-controlled 200kN servo-hydraulic test facility custom built by M/s BISS, Bangalore. A constant crosshead speed of 1 mm/min corresponding to an initial strain rate of 5.5×10^{-4}/s was used to carry out the tensile test. Four samples were tested at each condition and the average value obtained has been reported.

III. RESULTS

A. *Microstructure of Al-4.4Cu/TiB_2 Composite With and Without UT*

1. *As-cast condition*

The outcome of post-*in-situ* reaction ultrasonic treatment on reinforcement particles in Al-4.4Cu/2TiB_2 composites was analyzed and depicted in Figure 2. It can be seen from Figure 2(a) that in case of the material cast without ultrasonic treatment, the TiB_2 exhibits a hexagonal morphology with an average particle size of 950 ± 80 nm. The selected area diffraction (SAD)

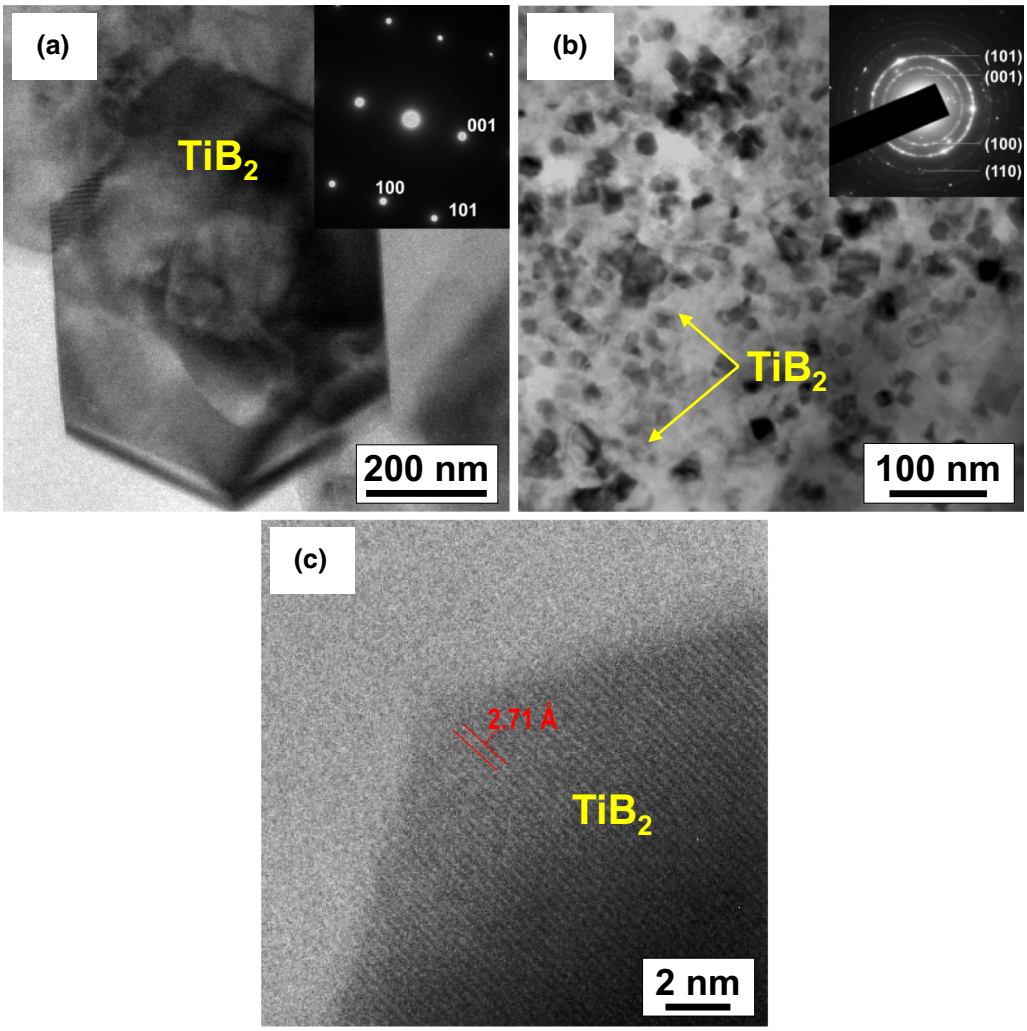

Fig. 2—TEM bright-field image of Al-4.4Cu/2TiB_2 composite (*a*) without and (*b* and *c*) with ultrasonic treatment.

pattern of particles prepared without ultrasonic treatment and acquired from ⟨010⟩ zone axis is shown as an inset of Figure 2(a). The indexed spot pattern (inset of Figure 2(a)) matches the standard lattice parameters for (001) and (101) planes of TiB_2 with inter planar spacing (d) of 2.2 and 3.3 Å, respectively. The observation of spot pattern (inset of Figure 2(a)) in composite without UT clearly indicates that the TiB_2 particles are in micron-sized range. Figure 2(b) represents the TEM images of Al-4.4Cu/2TiB_2 composite subjected to UT. In the case of composite with UT, the particles exhibit faceted morphology with an average particle size of 24 ± 13 nm. The continuous ring-type SAD pattern from the particles of composite with UT (inset of Figure 2(b)) further substantiates that the particles prepared with UT are in nano-range. Figure 2(c) shows high-resolution transition electron microscopy (HRTEM) image of an interface between TiB_2 particle and α-Al matrix in ultrasonic-treated composite. The interface was observed as free from pores, absence of brittle intermetallic phases like Al_3Ti, and other defects. It is expected that this clean interface would enable effective load transfer from matrix to reinforcement upon mechanical loading. The particle size reduction during post-*in-situ* reaction can be abbreviated using the effect of *the non-linear ultrasonic cavitation implosion theory*.[17] During occurrence of the cavitation implosion, extremely high temperature, pressure, and powerful shock waves are generated in the localized region[18] and the instantaneous pressure and temperature developed can be theoretically calculated to 23.58 atm. and 7800 °C, respectively. The details of the calculations are discussed elsewhere.[19–21] The instantaneous temperature and pressure build up in the localized region inside the melt can initiate the melting of TiB_2 from its sharp corners where the atoms having tangling bonds. During UT, successive implosions lead to dissolution of particles which later precipitate as nano-sized particles.[16] The powerful shock wave created during the cavitation implosion can clean the interface to improve the wettability between reinforcement particles and matrix.[3]

The optical microstructures of Al-4.4Cu alloy/Al-4.4Cu/2TiB_2 composite with and without UT conditions are shown in Figure 3. The base alloy Al-4.4Cu (Figure 3(a)) exhibits a typical coarse dendritic structure

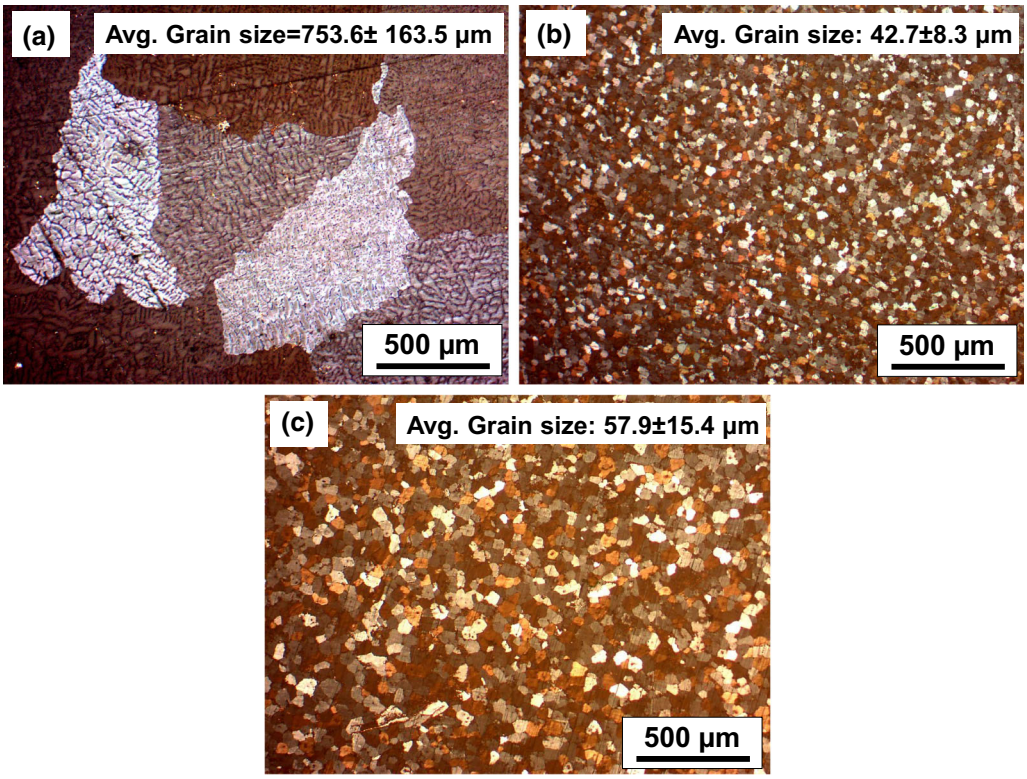

Fig. 3—Microstructure of (*a*) Al-4.4Cu alloy, Al-4.4Cu/2TiB_2 (*b*) without and (*c*) with UT.

with an average grain size of 753.67 ± 163.57 μm. The dendrites of primary α-Al present in the grain were observed to be elongated with an aspect ratio of 3.07 ± 0.18. The microstructure of Al-4.4Cu/TiB_2 composite without UT is depicted in Figure 3(b). It can be clearly seen that TiB_2 particles present in the material has aided in producing fine equiaxed grains which are devoid of dendrites. The average grain size of composite without UT was estimated to be 42.7 ± 8.3 μm. The microstructure of composite subjected to ultrasonic treatment also exhibits equiaxed grains (Figure 3(c)) however with a marginally increased grain size of 57.97 ± 15.42 μm. Incorporation of TiB_2 particles to Al-4.4Cu alloy has significant effect on its grain refinement. The presence of micron-sized TiB_2 particles were found to reduce the grain size of α-Al by 10- to 15-fold. Interestingly, ultrasonic treatment of Al-4.4Cu/TiB_2 composite has increased the grain size of α-Al marginally. Zhang *et al.*[22] reported that a low lattice mismatch between α-Al and TiB_2 in certain crystallographic planes such as $\{200\}_{Al}/\{10\bar{1}1\}_{TiB_2}$, $\{220\}_{Al}/\{11\bar{2}0\}_{TiB_2}$, $\{220\}_{Al}/\{10\bar{1}0\}_{TiB_2}$. Therefore, the ledges of TiB_2 particles exposing the matching planes between matrix and reinforcement can possess a lower interfacial energy to act as a heterogeneous nucleation site for α-Al. The grain refinement of Al-4.4Cu/2TiB_2 composites can be attributed to the lower crystallographic mismatch between α-Al and TiB_2 particles. When the composite melt is treated with ultrasonic waves, the non-linear effects of cavitation implosion can increase the volume fraction of particles by breaking down the micron-sized TiB_2 particles. However, in actual practice, all the TiB_2 particles existing in the melt may not initiate nucleation, only those particles which are active in the given melt condition can cause nucleation.[23] UT can enhance the number of active nucleant particles by cleaning the particle surface to increase the wettability and thus the potency of TiB_2 particles.[24] Furthermore, the pressure-pulse melting effect of cavitation implosion can enhance the nucleation rate. According to Clausius–Clayperon equation, the pressure increment instigated by cavitation implosion can produce localized undercooling of the melt.[24] Potency of TiB_2 particle to act as a nucleant can be further improved in the presence of such local undercooling. However, the impact of increased volume fraction of nucleant particle on the grain refinement process is not realized in ultrasonic-treated Al/TiB_2 composites. Alternatively, it can be assessed with the thermodynamic conditions and solidification behavior of composite melt.

The thermodynamic undercooling necessary for initiation of nucleation can be calculated using "Hemispherical Cap Model" as[25]

$$\Delta T_{fg} = \frac{4\sigma_{sl}}{\Delta S_v d}, \qquad [1]$$

where ΔT_{fg} is the undercooling for a particle size of d μm, σ_{sl} is the solid liquid interfacial energy, and ΔS_v is the entropy of fusion of metal. The values of σ_{sl} and ΔS_v have been reported to be 158 mJ/m^2 and 1.112×10^6 J/Km^3, respectively,[25] for Al alloys. Using Eq. [1], the theoretical undercooling required for

enabling heterogeneous nucleation on the surface of a 950-nm-sized particle was estimated to be 0.58 °C. As the particle size reduces to 20 nm, this theoretical value increases to 28 °C. The average grain size observed for Al-4.4Cu/2TiB_2 samples with TiB_2 particles of 950 and 20 nm sizes are ~ 43 and ~ 58 μm, respectively. The microstructural evolution can be justified as, even though the required undercooling is high for 20 nm TiB_2 particles, the pressure-pulse melting effect of cavitation implosion can provide necessary localized undercooling required for the nucleation and thus the grain refinement in ultrasonic-treated composites.

The FESEM microstructure shown in Figure 4(a) for Al-4.4Cu base alloy reveals that the inter-dendritic region of alloy comprises coarse $CuAl_2$ lamellae with an average size of 31.9 ± 8 μm. The aspect ratio of $CuAl_2$ particles present in the as-cast alloy was estimated to be 14.27 ± 2.59. From the micrograph of Al-4.4Cu/2TiB_2 composite cast without UT shown Figure 4(b), it can be inferred that the presence of micron-sized TiB_2 particles in Al-Cu matrix has reduced the thickness of $CuAl_2$ particles. The size and aspect ratio of the $CuAl_2$ particles or lamellae were estimated to be 18.57± 6.99 μm and 10.48 ± 1.53, respectively. In case of the composite produced with UT (Figure 4(c)), the size and aspect ratio of the $CuAl_2$ particle are reduced to 12.76 ± 4.86 μm and 7.59 ± 1.88, respectively. From the aforementioned observations, it can be clearly established that the thickness and aspect ratio of the $CuAl_2$ particles present in the base alloy decrease due to the presence of TiB_2 particles in the composite. The thickness and aspect ratio of $CuAl_2$ further get refined due to sonication of the composite.

The SEM micrograph of Al-4.4Cu/TiB_2 composite (without UT) shown in Figure 4(b) clearly reveals the presence of TiB_2 agglomerates in the material. In case of composite subjected to UT shown in Figure 4(c), the major fraction of nano-scale TiB_2 particles were found to be present along the grain boundary of α-Al matrix while, the remaining fraction of the TiB_2 particles were distributed in the matrix. The nano-sized TiB_2 particles in the grain boundaries were found to be in the form of small bands with an average thickness of 660 ± 130 nm (Zone 1). The particle dispersed zones were primarily observed near to the band-like agglomerate zone (Zone 2). Particle depleted zones (Zone 3) were observed at the core of the grain as shown in Figure 4(c). Similar observation has been reported by Mula *et al.*[17] in Al/Al_2O_3 nanocomposites. The refinement of eutectic $CuAl_2$ observed in Al-4.4Cu/TiB_2 composite can be explained by the presence of TiB_2 particles in the inter-dendritic region. The TiB_2 particles present in the inter-dendritic region can act as a barrier to the growth of eutectic phase thereby refining it. In the case of ultrasonic-treated composites, in addition to the growth pinning effect of TiB_2 particles, melt homogenization by ultrasonic treatment can also refine the eutectic phase.[23,26]

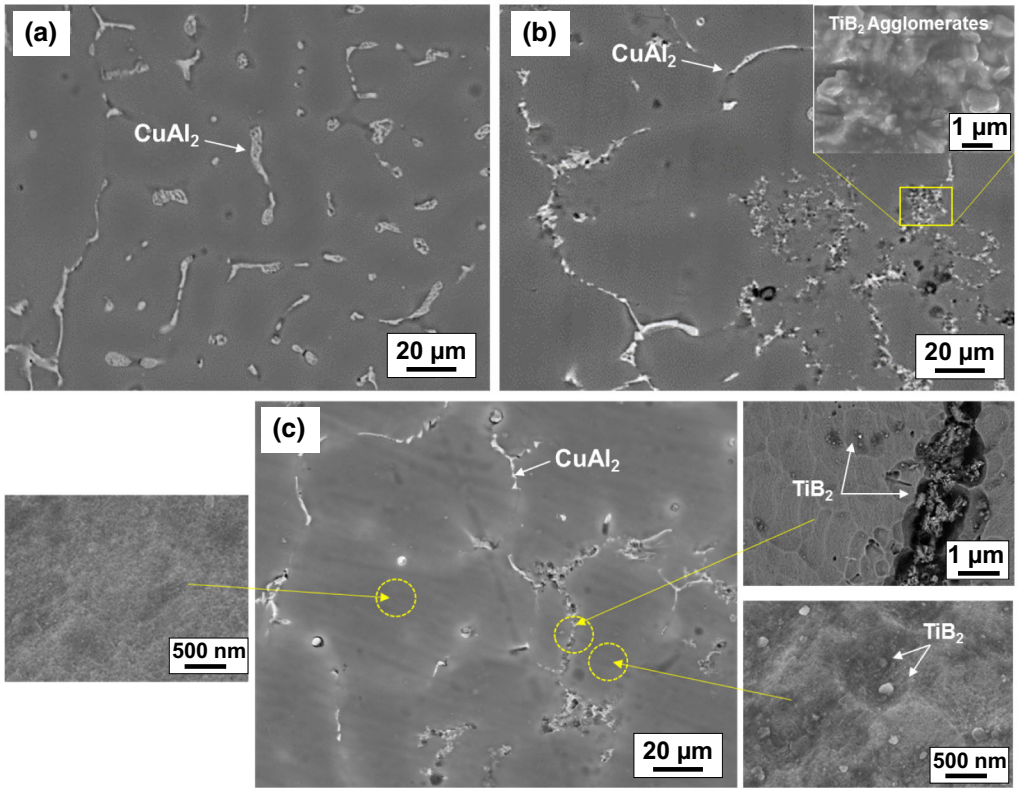

Fig. 4—FESEM micrograph of (*a*) Al-4.4Cu alloy, Al-4.4Cu/2TiB_2 composite (*b*) without and (*c*) with UT.

The salt-melt *in-situ* reaction generates micron-sized TiB_2 particles and the solidification of such composites without any influence from external fields like ultrasonic treatment results in agglomeration of TiB_2 particles along the grain boundaries of α-Al. In case of the composite cast with UT, though the major fraction of nano-sized TiB_2 particles are present as a chain-like structure along the grain boundaries, the remaining fraction of particles were dispersed in the grains. The agglomeration of TiB_2 nanoparticles and formation of band-like structure along the grain boundaries can be attributed to segregation of TiB_2 nano particles at the solidification front. The particle segregation behavior can be explained using Hamaker's constant. Recently, Xu *et al.*[27] proposed a new approach for prediction of spontaneous engulfment and pushing of nanoparticles based on the Van der Waals potential of the system and it can be written as

$$W_{vdw} = -\left[\frac{\left(\sqrt{A_{Solid}} - \sqrt{A_{Liquid}}\right)\left(\sqrt{A_{nanoparticle}} - \sqrt{A_{Liquid}}\right)}{6} \times \left\{\frac{R}{D} + \frac{R}{2R+D} + \ln\frac{D}{2R+D}\right\}\right], \quad [2]$$

where A_{Solid}, A_{Liquid}, and $A_{nanoparticle}$are Hamaker constant of solid metal, liquid melt, and nanoparticles, respectively, R is the radius of nanoparticle, and D is the distance between the solidification front and the nanoparticle. According to this model, the spontaneous engulfment of the nanoparticle occurs only when the Van der Waals potential (W_{vdw}) of the system is negative. It is well established that Hamaker constant of solid metal A_{Solid} is always larger than the liquid meltA_{Liquid}; hence, spontaneous engulfment is narrowed down to constant of the nanoparticle $A_{nanoparticle}$. For TiB_2 particles, Hamaker constant is 256[27] which is lower than that of liquid Al (Hamaker Constant = 266)[27] and hence results in positive Van der Waals potential. This implies that spontaneous engulfment is not possible in Al-TiB_2 system. When the Van der Waals force is positive, repulsive force pushes the particles further away from the solidification while the viscous drag force acts to slow it down for engulfment process. For the viscous engulfment process to be active, the advancing velocity of the solidification front must be higher than a certain critical velocity. According to model proposed by Xu *et al*,[27] for Al-TiB_2 nanocomposite with TiB_2 particles in the range of 20 to 30 nm, the critical velocity is 74 to 110 μm/s. Such a large solidification velocity cannot be achieved in regular permanent mold processes wherein solidification velocity in the order of 1 to 2 μm/s. This implies that engulfment of nanoparticles can be achieved only with the aid of Brownian capture process. For this process to occur, Brownian potential of the nanoparticles should overcome the energy barrier created by the positive Van der Waals potential of the system. Hence, the nanoparticle spontaneously moves towards the solidification front for Brownian capture[28]:

$$-\left[\frac{\left(\sqrt{A_{Solid}} - \sqrt{A_{Liquid}}\right)\left(\sqrt{A_{nanoparticle}} - \sqrt{A_{Liquid}}\right)}{6} \times \left\{\frac{R}{D} + \frac{R}{2R+D} + \ln\frac{D}{2R+D}\right\}\right] \le \left(\frac{kT}{2}\right). \quad [3]$$

From Table I, it is clear that Brownian capture of TiB_2 nanoparticle during solidification of Al melt is possible only when size of TiB_2 is equal to or less than 20 nm. Experimental observation of small fraction of TiB_2 nanoparticle in the α-Al grain supports the Brownian capture process (Figure 3(c)). Aforementioned results suggest that though ultrasonic treatment has the potency to disperse the TiB_2 nanoparticle uniformly in Al melt, the solidification characteristic of Al-TiB_2 composite hinders complete dispersion of particle along the matrix.

2. *Microstructure of peak-aged samples*

TEM micrographs of Al-4.4Cu alloy and Al-4.4Cu/2TiB_2 composites with and without UT in peak-aged condition are shown in Figure 5. Bright-field TEM images of Al-4.4Cu base alloy in its peak-aged condition depict (Figure 5(a)) the presence of 119 ± 13.7 nm size plate like θ' precipitates. The micrograph also confirms that absence of GP zones in the material. Similarly in peak-aged composite without UT (Figure 5(b)), the needle-type θ' precipitates were found to have a refined arm length. The length of needle-shaped θ' precipitate in the composite without UT was estimated to be 75.4 ± 24 nm which is lesser than that observed in the base alloy. Further, the fraction of θ' precipitate was found to be considerably higher in the composite without UT. In case of peak-aged composite subjected to UT (Figure 5(c)), the θ' precipitates were found to be further refined with an average size of 46.39 ± 9.6 nm with a concomitant increase in the volume fraction. The observation on θ' precipitates made here concurs well with the results reported by Dong *et al*. for Al-Cu/CNT nanocomposites.[18]

B. *Mechanical Properties of Al-4.4Cu/2TiB₂ With and Without UT*

Typical room temperature engineering stress–strain curve of Al-4.4Cu alloy and Al-4.4Cu/2TiB_2 composites with and without UT for different heat treatment conditions are presented in Figure 6. The mechanical property data are summarized in Table II for ready inference. The stress–strain curves for the as-cast material are compared in Figure 6(a). The base alloy Al-4.4Cu in the as-cast condition exhibits an average yield and ultimate tensile strength (UTS) of ~ 94 and ~ 222 MPa, respectively, with an elongation of 17 pct. The formation of micron-sized TiB_2 particles in the base alloy due to salt-melt *in-situ* reaction increased the yield strength of the material to ~ 129 MPa with concomitant decrease in percent elongation to ~ 8.9 pct as shown in

Figure 6(a). Though the yield strength of the base alloy was increased due to the *in-situ* formation of TiB_2 particles, no significant change was observed in the UTS indicating that the micron-scale TiB_2 particles does not enhance the strain hardenability of material. Further, from Figure 6(a), it can be inferred that 5-minute ultrasonic treatment after *in-situ* reaction has enhanced the yield and tensile strength to 184 and 333 MPa without any appreciable decrease in ductility when compared to the base alloy Al-4.4Cu.

Table I. Energy Barrier and Brownian Potential in Al-TiB_2 System

Parameters	Value	Reference
A_{solid} (zJ)	333	27
A_{Liquid} (zJ)	266	
$A_{Nanoparticle}$ (zJ)	256	
Radius (nm)	20	
Energy Barrier, kT/2 (zJ)	6.22	
Brownian Potential (zJ)	6.26	

The stress–strain behavior of Al-4.4Cu alloy and composites with and without UT in peak-aged condition are presented in Figure 6(b). As expected, age hardening has enhanced the strength of all the materials. The variation in the strength and ductility observed after peak aging is similar to that obtained in the as-cast condition, *i.e.*, the composite subjected to 5-minute UT exhibits better strength when compared to the base alloy and the composite without UT. Ductility of all the materials in peak-aged condition was observed to be higher than that the as-cast counterparts.

IV. DISCUSSION

A. *Structure–Property Correlation Analysis*

1. *Strengthening mechanisms in the as-cast Al-4.4Cu/TiB_2 composites*

The theoretical yield strength of the as-cast Al-4.4Cu/$2TiB_2$ composites can be estimated by considering the strengthening contributions from grain refinement, intermetallic particles, and reinforcement particles[29] as per the following equation

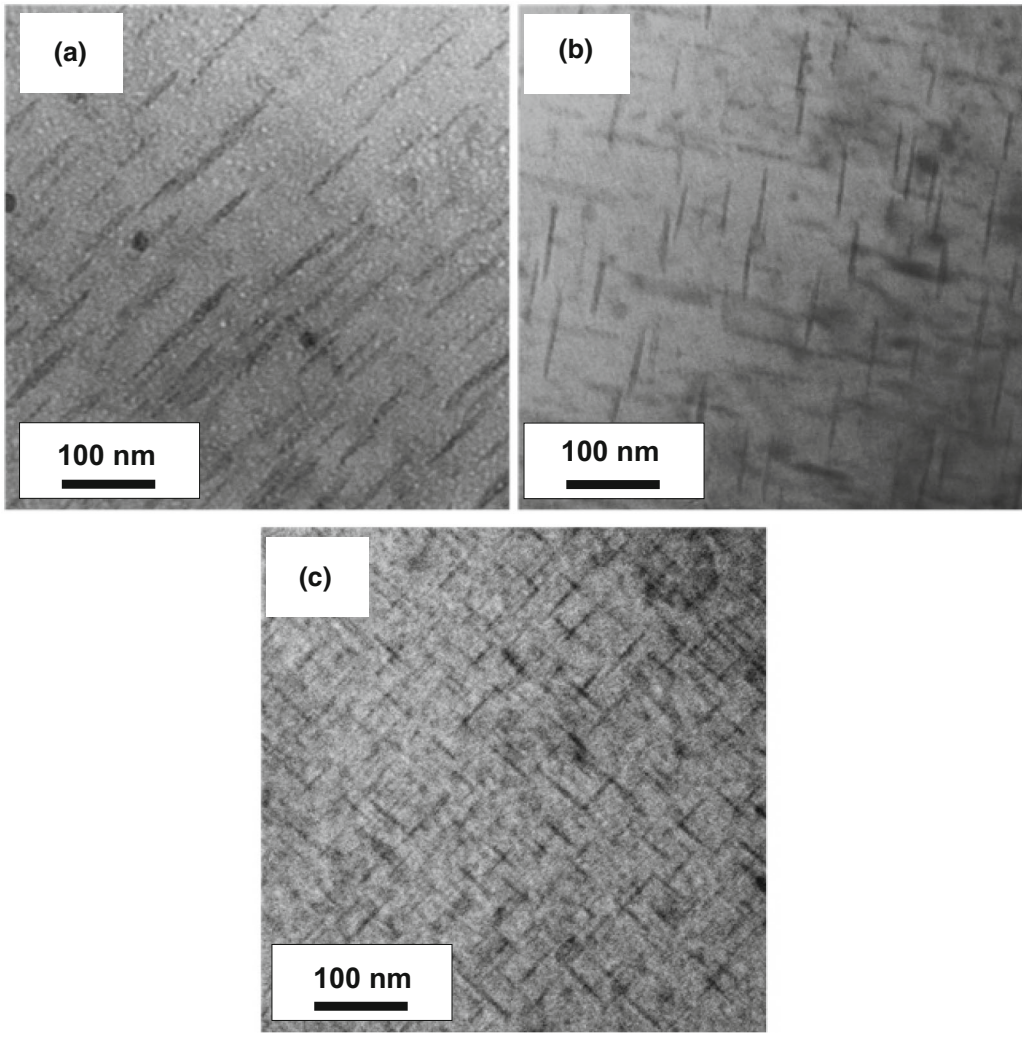

Fig. 5—TEM bright-field images of (*a*) Al-4.4Cu alloy, Al-4.4Cu/$2TiB_2$ composite (*b*) without UT and (*c*) with UT in peak-aged condition.

$$\sigma_y = \sigma_m + \frac{k}{\sqrt{d}} + \sigma_{Reinf}, \quad [4]$$

where σ_m is the strengthening contribution from the matrix, k is the Hall–Petch slope and it is 0.13 MPa $m^{\frac{1}{2}}$ for Al-4.4Cu alloy,[30] d is the grain size, $\sigma_{in}$is strengthening contribution from $CuAl_2$ particles, and $\sigma_{Reinf}$is the contributions from reinforcement particles and can be calculated as[29]

$$\sigma_{Reinf} = \sqrt{\sigma_{oro}^2 + \sigma_{CTE}^2 + \sigma_{Geo}^2 + \sigma_{Load}^2}, \quad [5]$$

where σ_{oro} is increment in stress required to pass the dislocation through the array of particles, σ_{CTE} is the stress developed due to the difference in coefficient of thermal mismatch between matrix and reinforcement, σ_{Geo} is stress contribution due to strain gradient associated with geometrically necessary dislocations required to accommodate the plastic deformation mismatch between matrix and reinforcement particles, and σ_{Load} is the influence of load transfer effect between particles and matrix.

The resistance offered by TiB_2 particles to the passage of dislocations can be estimated using Ashby–Orowan equation[31]:

$$\sigma_{Oro} = \frac{2mGb\ln\{\phi/2b\}}{[(1.18)4\pi(\lambda - \phi)]}, \quad [6]$$

where m is the Taylor factor, G is the shear modulus, b is the Burgers vector, ϕ is reinforcement particle size, and λ is the planar inter particle separation which is given by $\phi/\sqrt{V_p}$, where V_p is the volume fraction of reinforcement particles.

Strengthening contribution derived from thermal mismatch between matrix and reinforcement particle is given by[32]

$$\sigma_{CTE} = \eta Gb\rho^{1/2}, \quad [7]$$

where η is a constant of order 1, and ρ is the dislocation density which can be calculated as[33]

$$\rho = \frac{12\Delta\alpha\Delta T V_p}{b\phi(1 - V_p)}, \quad [8]$$

where $\Delta\alpha$ is the coefficient of thermal mismatch difference of matrix alloy and reinforcement, and ΔT is the difference in testing and processing temperature. The contribution from the geometrically necessary dislocations can be estimated using Eq. [9][34,35]

$$\sigma_{Geo} = \beta G\sqrt{\frac{V_p \in b}{\phi}}, \quad [9]$$

where β is a geometric factor with a numerical value of 0.2 and ϵ is the plastic strain of matrix. Finally, the

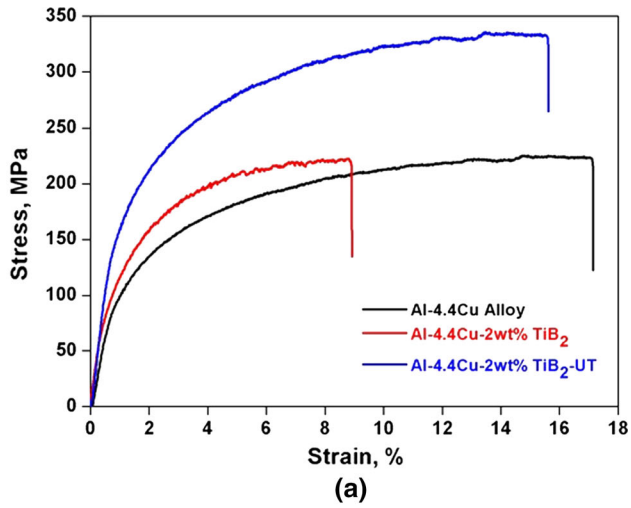

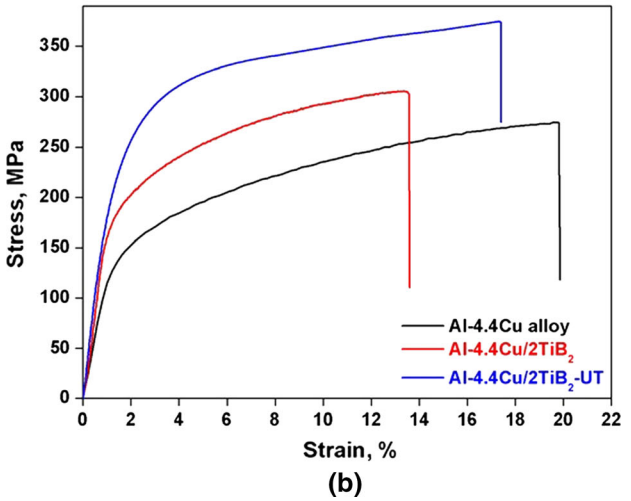

Fig. 6—Stress–strain behavior of Al-4.4Cu alloy and composites with and without UT in the (*a*) as-cast and (*b*) peak-aged condition.

Table II. Tensile Results of Alloy and Composites With and Without UT

Sample	Condition	0.2 Pct Yield Strength (MPa)	Ultimate Tensile Strength (MPa)	Elongation (Percent)
Al-4.4Cu Alloy	As Cast	94.43 ± 3.4	222.1 ± 4.8	17.1 ± 0.3
	T6	120.4 ± 4.2	275.3 ± 3.2	19.8 ± 0.7
Al-4.4Cu/2TiB_2	As Cast	129.4 ± 6.5	224.3 ± 5.6	8.9 ± 1
	T6	159.2 ± 3.1	304.9 ± 3.1	13.6 ± 0.9
Al-4.4Cu/2TiB_2-UT	As Cast	184.3 ± 3.6	333.8 ± 5.3	15.6 ± 0.5
	T6	230.1 ± 5.3	375 ± 2.3	17.4 ± 0.4

contribution from load transfer effect can be calculated as[28]

$$\sigma_{\text{Load}} = 0.5s\sigma_{\text{m}}V_{\text{p}}, \quad [10]$$

where s is the aspect ratio of particles.

The values of various parameters used for estimating the strength contribution from the aforementioned terms are listed in Tables III and IV. The effect of particle size on the strength contribution from Orowan looping, CTE mismatch, geometrical dislocations, and load transfer using Eqs. [4] through [10] are shown in Figure 7. For the calculation purpose, the agglomerates of TiB_2 particles in the ultrasonic-treated composites are considered as bigger size particles of ~ 400 nm in size. From Figure 7, it can be clearly seen that the strength contribution from coefficient of thermal expansion mismatch, Orowan loops, and geometrically necessary dislocations decreases exponentially as the particle size is increased. Among the abovementioned strengthening mechanisms, the contribution from the Orowan loops can be observed to higher when the particle sizes are less than 100 nm. As the particle size increases beyond 100 nm, the strength contribution due to CTE mismatch is higher. Further, from Figure 8, it can also be inferred that the strength contribution from load transfer mechanism is marginal and it does not vary with increasing particle size.

The yield strength of Al-44.4Cu/TiB_2 composites calculated theoretically correlate well with the experimental values as shown in Table V. Further, the theoretical model substantiates that the reinforcement particle size have significant effect on the yield strength of Al-44.4Cu/TiB_2 composites. It can be rationalized that the presence of nanoparticles enhances the strength of Al-4.4Cu matrix due to Orowan looping, CTE mismatch effect, and the generation of geometrically necessary dislocations. In addition, TiB_2 particles refine the grain size of Al matrix and thereby provide Hall–Petch strengthening.

Table III. Parameters Used for Calculation of Strengthening Derived from Precipitates

Parameters	Samples	Value
r	Al-4.4Cu alloy	15.2 ± 2.3 nm
	Al-4.4Cu/2TiB_2	12 ± 0.91 nm
	Al-4.4Cu/2TiB_2-UT	0.3893 ± 0.13 nm
V_θ	Al-4.4Cu alloy	0.041
	Al-4.4Cu/2TiB_2	0.0528
	Al-4.4Cu/2TiB_2-UT	0.0596

Table IV. Parameters Used for Theoretical Calculation of Increments in Yield Strength

Parameters	Value	Reference
Vp	0.0124	Present work
b	0.286 nm	28
G_{m}	27 GPa	
α of Al	24×10^{-6} K^{-1}	
α of TiB_2	7.8×10^{-6} K^{-1}	
ΔT	730 °C	PW
ϵ	0.1	35
s	1	28
m	3.1	35
k_{y}	0.13 MPa $m^{-1/2}$	30
a_{Al}	0.405 nm	37
$a_{\theta'}$	0.406 nm	
γ_{APB}	0.03 Jm^{-2}	41
G_{ppt}	29.2 GPa	39
v	0.33	28

2. *Strengthening mechanisms in precipitation-hardened Al-4.4Cu/TiB_2 composites*

Strength of precipitation-hardened alloy is primarily governed either by dislocation bypass or shear mechanism. In shearing mechanism, three factors contribute to increase in yield strength: coherency, modulus mismatch, and order strengthening. Coherency strengthening is due to the strain-field interactions between a coherent precipitate and dislocation. The contribution of coherency strengthening can be calculated as[36]

$$\Delta\sigma_{\text{coh}} = 2.6m(G_{\text{m}}\varepsilon)^{3/2}\left(\frac{rV_\theta}{0.5G_{\text{m}}b}\right)^{1/2}, \quad [11]$$

where $\varepsilon = 2/3(\Delta a/a)$ is constrained lattice parameter mismatch. a is the lattice parameter of aluminum and Δa is the difference in the lattice parameter between matrix and precipitate phase.[37]

The lattice parameter mismatch between the coherent precipitate and matrix creates a strain field at the interface and the interaction of dislocations with these strain fields increases the yield strength. The difference in shear modulus between the precipitate and matrix alters the line tension of the mobile dislocation and causes an associated increase in strength which is known as modulus strengthening. The increment in strength through modulus mismatch can be calculated as[38]

$$\Delta\sigma_{\text{mod}} = 0.0055m(\Delta G)^{3/2}\left(\frac{2V_\theta}{G_{\text{m}}}\right)^{1/2}\left(\frac{r}{b}\right)^{\left(\frac{3M-2}{2}\right)}, \quad [12]$$

where ΔG is difference in shear modulus between matrix (G_{m}) and precipitate (G_{ppt}), M is a constant with a value of 0.85, and r is the mean diameter of precipitate.[38,39]

Strengthening due to ordering is because of the formation of anti-phase boundary (APB), which occurs when a matrix dislocation shears an ordered precipitate. The increase in the yield strength due to ordering is given by[40]

$$\Delta\sigma_{\text{ord}} = 0.81m\frac{\gamma_{\text{APB}}}{2b}\sqrt{\frac{3\pi V_\theta}{8}}, \quad [13]$$

where γ_{APB} is the anti-phase boundary energy, and V_θ is the volume fraction of precipitate phase.[41]

Modulus and coherency strengthening mechanisms occur simultaneously and their net effect can be expressed in a linear fashion.[42] However, the larger of (a) the sum of coherency strengthening and modulus strengthening or (b) order strengthening is the total strength increment due to dislocation shearing.[36] The

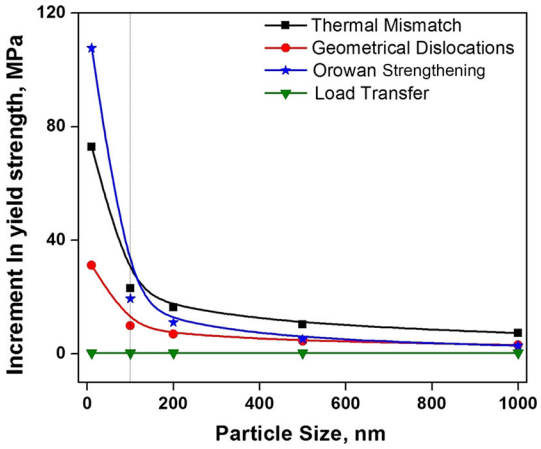

Fig. 7—Reinforcement particle size dependencies on strengthening mechanism.

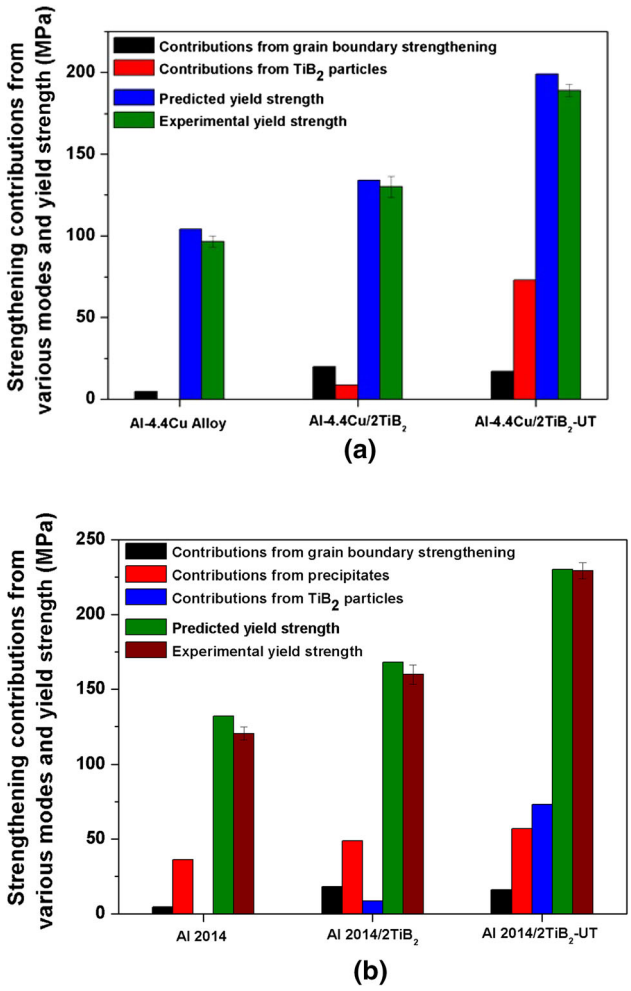

Fig. 8—Strengthening contributions from reinforcement particles, intermetallic phase, and Hall–Petch effect in the (*a*) as-cast condition and (*b*) peak-aged condition.

reason behind the selection of larger contribution among the two modes is that they are sequential in action, *i.e.,* the coherency and modulus strengthening occurs at the interface just before the dislocation shears the precipitate. The ordering occurs during shearing. Coherency and modulus mismatch strengthening has the highest contribution towards yield strength increment when the dislocation interaction is close to the precipitate interface. However, the strengthening due to order strengthening is in its maximum when the dislocation has sheared half of the precipitate.[36,38,43]

In addition, the precipitates can contribute to the yield strength by Orowan mechanism. The contribution from this mechanism can be calculated as[38]

$$\Delta\sigma_{\text{Oro-PPT}} = m\frac{0.4G_{\text{m}}b}{\pi\sqrt{1-\upsilon}}\frac{\ln(2\bar{r}/b)}{\lambda_{\text{e-e}}}, \qquad [14]$$

where υ is Poisson ratio of matrix material, and $\bar{r} = \sqrt{2/3}\langle r\rangle$, $\lambda_{\text{e-e}}$ is the mean edge-to-edge inter-precipitate spacing and given by Reference 43 $\lambda_{\text{e-e}} = r\left[\left(\frac{3\pi}{4V_\theta}\right)^{1/2} - 1.64\right]$. By using the necessary data given in Tables III and IV, the contributions were calculated. The increment in strength of matrix due to the presence of precipitate phases was calculated using Eqs. [11] through [14].

For adequately large precipitates, the shearing stress is larger than the stress required for the dislocation to bypass the precipitates. In such cases, the lowest among the shearing stress and Orowan stress is considered as the operative mechanism.[44] For the present experimental conditions, the calculated value of Orowan looping is smaller than the contribution from dislocation shearing. Therefore, dislocation bypassing mechanism is considered as the operating mechanisms of strengthening in peak-aged Al-Cu alloys. Hence, the total strengthening contribution from precipitation hardening can be calculated as

$$\sigma_{\text{PPT}} = \sigma_{\text{Oro-PPT}}. \qquad [15]$$

The yield strength of age-hardened composite material can be calculated as[45]

$$\sigma_{\text{y}} = \sigma_{\text{m}} + \frac{k}{\sqrt{d}} + \sigma_{\text{Reinf}} + \sigma_{\text{PPT}}. \qquad [16]$$

The role of TiB_2 particles, intermetallic phases, and grain refinement on the strengthening contribution of both the as-cast and peak-aged samples are compared in Figure 8.

It can be observed that in case of base alloy, the contribution due to grain boundary strengthening is comparable in the as-cast as well as peak-aged condition. However, in the peak-aged condition, the contribution to the strength due to the presence of fine coherent Al_2Cu intermetallic precipitates are much higher when compared to the as-cast material.

For the Al-4.4Cu alloy reinforced with micron-sized TiB_2 particles, the strengthening contribution derived from both Al_2Cu particles and grain boundary strengthening is higher than that of monolithic alloy. The strengthening due to grain boundary shows a marginal reduction in the peak-aged condition when compared to

Table V. Comparison of Theoretical Prediction of Yield Strength and Experimental Values

Material	As Cast		Peak-Aged Condition	
	Theoretical Prediction (MPa)	Experimental Value (MPa)	Theoretical Prediction (MPa)	Experimental Value (MPa)
Al-4.4Cu-Alloy	104.89	94.43 ± 3.4	132.59	120.40 ± 4.2
Al-4.4Cu/2TiB_2	134.87	129.40 ± 6.5	168.80	159.20 ± 3.1
Al-4.4Cu/2Ti-B_2-UT	199.28	184.30 ± 3.6	240.38	230.10 ± 5.3

the as-cast condition. This can be attributed to the marginal grain coarsening during solution treatment. The eutectic particle refinement and grain size reduction due to the presence of TiB_2 particles contribute to the strength increment in the as-cast composite. In addition, the peak-aged composite samples shows fourfold increase in yield strength when compared to the as-cast monolithic alloy. This can be attributed to the presence of Al_2Cu intermetallic precipitates. The presence of TiB_2 particles in Al-4.4Cu alloy increases the dislocation density and thereby increases the possible nucleation sites for precipitation of Al_2Cu particles. The increased number of nucleation events leads to refinement in $CuAl_2$ precipitate size which enhances the strengthening contribution.

In the case of ultrasonic-treated composites, further refinement of the eutectic $CuAl_2$ particles enhances the yield strength, while the slight coarsening in the grain size reduces the grain boundary strengthening of the as-cast nanocomposite. In peak-aged condition, the ultrasonic-treated composite exhibits the highest strengthening contribution from the coherent precipitates with a marginal reduction in grain boundary strengthening when compared to the as-cast condition. The refinement of TiB_2 particle to nano-scale further enhances the dislocation density and leads to nucleation of more number of $CuAl_2$ precipitates than the monolithic alloy and micro-composites. The theoretical predictions of yield strength and experimental values are given Table V. It can be observed that the theoretical yield strength estimates correlate well with the experimental values of for the alloy and the composites. For peak-aged samples, the strengthening models contemplated indicates that, along with the strengthening contributions induced by the reinforcement particles, the precipitation of coherent $CuAl_2$ intermetallic particles are contributing to yield strength through dislocation bypassing.

V. SUMMARY

In this study, the results of microstructural features, mechanical properties especially Tensile behavior, structure–property correlation of Al-4.4Cu/2TiB_2 micro- and nanocomposites in the as-cast and peak-aged conditions have been presented. The strength of Al-4.4Cu monolith alloy enhances considerably at the cost of ductility by incorporating the micron-sized *in-situ* TiB_2 particles. However, the particle size reduction of TiB_2 particles in the regime of ~ 20 nm substantially enhances the strength along with matrix ductility retention. The as-cast yield strength of the base alloy was increased due to the *in-situ* formation of TiB_2 particles, and no significant change was observed in the UTS indicating that the micron-scale TiB_2 particles does not enhance the strain hardenability of material. The as-cast tensile yield strength of matrix alloy increased by > 90 pct while retaining 91 pct ductility of the matrix due to incorporation of nano-sized TiB_2 particles. The precipitation hardening of composite added further strengthening. As a combined effect of nano-TiB_2 and T6 heat treatment, the yield strength of the as-cast Al-4.4Cu alloy increased from 86 to 230 MPa without any secondary processing like rolling. In as-cast condition, grain refinement in the matrix, Orowan looping, CTE mismatch, generation of geometrical necessary dislocations, and load transfer characteristics of the TiB_2 particles contribute to the strength. However, in the precipitation-hardened samples along with the contributions from grain boundary strengthening due to the presence of reinforcement particles, dislocation bypassing through the precipitates enhances the strength.

On the microstructural analysis side, it can be observed that a major fraction of nano-scale TiB_2 particles were found to be present along the grain boundary of α-Al matrix, while the remaining fraction of the TiB_2 particles were distributed in the matrix. The nano-sized TiB_2 particles in the grain boundaries were found to be in the form of small bands and particle dispersed zones were primarily observed near to the band-like agglomerate zone. A particle depleted zones were observed at the core of the grain. The complete dispersion of TiB_2 particles in liquid Al melt was difficult because of the positive Van der Waals potential created by the difference in Hamaker's constant between TiB_2 and liquid Al. Further, TiB_2 particles present in the material aids in transforming dendritic grains into fine equiaxed ones in both the composite samples prepared without and with UT.

FUNDING

This research work is supported by the Directorate of Naval Research Board, Govt. of India (Grant No: DNRD/05/4003/NRB/292) and CSIR-India (Award No: 08/473(0006)/2015 EMR-1).

REFERENCES

1. K.R. Ravi, J. Nampoothiri, and B. Raj: *Nanotechnology for Energy Sustainability*, Wiley-VCH Verlag GmbH & Co. KGaA, Weinheim, 2017, pp. 831–56.
2. C. Borgonovo, D. Apelian, and M.M. Makhlouf: *JOM*, 2011, vol. 63, pp. 57–64.
3. Y. Yang and J. Lan: *X. Li*, 2004, vol. 380, pp. 378–83.
4. R. Casati and M. Vedani: *Metals*, 2014, vol. 4, pp. 65–83.
5. P. Henrique, C. Camargo, K.G. Satyanarayana, and F. Wypych: *Mater. Res.*, 2009, vol. 12, pp. 1–39.
6. K.B. Nie, X.J. Wang, K. Wu, X.S. Hu, and M.Y. Zheng: *Mater. Sci. Eng. A*, 2012, vol. 540, pp. 123–29.
7. O. Kudryashova and S. Vorozhtsov: *JOM*, 2016, vol. 68, pp. 1307–11.
8. P. Padhi, B.N. Dash, and S.K. Kar: *J. Nanotechnol.*, 2011, vol. 2011, pp. 1–4.
9. D. Yuan, X. Yang, S. Wu, S. Lü, and K. Hu: *J. Mater. Process. Technol.*, 2019, vol. 269, pp. 1–9.
10. M. Estruga, L. Chen, H. Choi, X. Li, and S. Jin: *ACS Appl. Mater. Interfaces*, 2013, vol. 5, pp. 8813–19.
11. R. Raghu, J. Nampoothiri, and T.S. Kumar: *Measurement*, 2018, vol. 129, pp. 389–94.
12. S.L. Pramod, S.R. Bakshi, and B.S. Murty: *J. Mater. Eng. Perform.*, 2015, vol. 24, pp. 2185–207. https://doi.org/10.1007/s11665-015-1424-2.
13. S. Lakshmi, L. Lu, and M. Gupta: *J. Mater. Process. Technol.*, 1998, vol. 73, pp. 160–66.
14. S. Bhogi, J. Nampoothiri, K.R. Ravi, and M. Mukherjee: *Mater. Sci. Eng. A*, 2017, vol. 685, pp. 131–38.
15. J. Nampoothiri, B. Raj, and K.R. Ravi: *Trans. Indian Inst. Met.*, 2015, https://doi.org/10.1007/s12666-015-0653-2.
16. J. Nampoothiri, R.S. Harini, S.K. Nayak, B. Raj, and K.R. Ravi: *J. Alloys Compd.*, 2016, vol. 683, pp. 370–78.
17. S. Mula, P. Padhi, S.C. Panigrahi, S.K. Pabi, and S. Ghosh: *Mater. Res. Bull.*, 2009, vol. 44, pp. 1154–60.
18. D.H. Nam, Y.K. Kim, S.I. Cha, and S.H. Hong: *Carbon N. Y.*, 2012, vol. 50, pp. 4809–14.
19. J.R.G. Sander, B.W. Zeiger, and K.S. Suslick: *Ultrason. Sonochem.*, 2014, vol. 21, pp. 1908–15.
20. J.H. Bang and K.S. Suslick: *Adv. Mater.*, 2010, vol. 22, pp. 1039–59.
21. K.S. Suslick, Y. Didenko, M. Fang, T. Hyeon, K. Kolbeck, W.B. McNamara, M.M. Mdleleni, and M. Wong: *Philos. Trans. R. Soc.*, 1999, vol. 357, pp. 335–53.
22. M.X. Zhang, P.M. Kelly, M.A. Easton, and J.A. Taylor: *Acta Mater.*, 2005, vol. 53, pp. 1427–38.
23. J. Nampoothiri, B. Raj, and K.R. Ravi: *Trans. Indian Inst. Met.*, 2015, vol. 68, pp. 1101–06.
24. T.V. Atamanenko, D.G. Eskin, L. Zhang, and L. Katgerman: *Metall. Mater. Trans. A*, 2010, vol. 41A, pp. 2056–66.
25. A.L. Greer, A.M. Bunn, A. Tronche, P.V. Evans, and D.J. Bristow: *Acta Mater.*, 2000, vol. 48, pp. 2823–35.
26. R. Thavamani, V. Balusamy, J. Nampoothiri, R. Subramanian, and K.R. Ravi: *J. Alloys Compd.*, 2018, vol. 740, pp. 870–78.
27. J.Q. Xu, L.Y. Chen, H. Choi, and X.C. Li: *J. Phys. Condens. Matter*, 2012, vol. 24, p. 255304.
28. M. Wang, D. Chen, Z. Chen, Y. Wu, F. Wang, N. Ma, and H. Wang: *Mater. Sci. Eng. A*, 2014, vol. 590, pp. 246–54.
29. Z. Száraz, Z. Trojanová, M. Cabbibo, and E. Evangelista: *Mater. Sci. Eng. A*, 2007, vol. 462, pp. 225–29.
30. T. Shanmugasundaram, B.S. Murty, and V. Subramanya Sarma: *Scr. Mater.*, 2006, vol. 54, pp. 2013–17.
31. V. Udhayabanu, K.R. Ravi, and B.S. Murty: *Mater. Sci. Eng. A*, 2013, vol. 585, pp. 379–86.
32. V. Udhayabanu, K.R. Ravi, K. Murugan, D. Sivaprahasam, and B.S. Murty: *Metall. Mater. Trans. A*, 2011, vol. 42A, pp. 2085–93.
33. R.J. Arsenault and N. Shi: *Mater. Sci. Eng.*, 1986, vol. 81, pp. 175–87.
34. S. Scudino, G. Liu, K.G. Prashanth, B. Bartusch, K.B. Surreddi, B.S. Murty, and J. Eckert: *Acta Mater.*, 2009, vol. 57, pp. 2029–39.
35. D. Poirier, R.A.L. Drew, M.L. Trudeau, and R. Gauvin: *Mater. Sci. Eng. A*, 2010, vol. 527, pp. 7605–14.
36. H. Wen, T.D. Topping, D. Isheim, D.N. Seidman, and E.J. Lavernia: *Acta Mater.*, 2013, vol. 61, pp. 2769–82.
37. S. Hu, M. Baskes, M. Stan, and L. Chen: *Acta Mater.*, 2006, vol. 54, pp. 4699–4707.
38. M.E. Krug, Z. Mao, D.N. Seidman, and D.C. Dunand: *Acta Mater.*, 2014, vol. 79, pp. 382–95.
39. Y.C. Waung, D.E. Beskos, and W. Sachse: *J. Mater. Sci.*, 1975, vol. 10, pp. 109–12.
40. C. Booth-Morrison, D.C. Dunand, and D.N. Seidman: *Acta Mater.*, 2011, vol. 59, pp. 7029–42.
41. H.I. Aaronson, J.B. Clark, and C. Laird: *Met. Sci. J.*, 1968, vol. 2, pp. 155–58.
42. J.Y. He, H. Wang, H.L. Huang, X.D. Xu, M.W. Chen, Y. Wu, X.J. Liu, T.G. Nieh, K. An, and Z.P. Lu: *Acta Mater.*, 2016, vol. 102, pp. 187–96.
43. D.N. Seidman, E.A. Marquis, and D.C. Dunand: *Acta Mater.*, 2002, vol. 50, pp. 4021–35.
44. C.B. Fuller, D.N. Seidman, and D.C. Dunand: *Acta Mater.*, 2003, vol. 51, pp. 4803–14.
45. M. Tabandeh-Khorshid, J.B. Ferguson, B.F. Schultz, C. Kim, K. Cho, and P.K. Rohatgi: *Mater. Des.*, 2016, vol. 92, pp. 79–87.